

Copper interstitial recombination centers in Cu_3N

Ye Sheng Yee,¹ Hisashi Inoue,² Adam Hultqvist,³ David Hanifi,⁴ Alberto Salleo,⁵ Blanka Magyari-Köpe,¹ Yoshio Nishi,¹ Stacey F. Bent,³ and Bruce M. Clemens⁵

¹*Department of Electrical Engineering, Stanford University, Stanford, California 94305, USA*

²*Department of Applied Physics, Stanford University, Stanford, California 94305, USA*

³*Department of Chemical Engineering, Stanford University, Stanford, California 94305, USA*

⁴*Department of Chemistry, Stanford University, Stanford, California 94305, USA*

⁵*Department of Materials Science and Engineering, Stanford University, Stanford, California 94305, USA*



(Received 3 March 2017; revised manuscript received 4 March 2018; published 4 June 2018)

We present a comprehensive study of the earth-abundant semiconductor Cu_3N as a potential solar energy conversion material, using density functional theory and experimental methods. Density functional theory indicates that among the dominant intrinsic point defects, copper vacancies V_{Cu} have shallow defect levels while copper interstitials Cu_i behave as deep potential wells in the conduction band, which mediate Shockley-Read-Hall recombination. The existence of Cu_i defects has been experimentally verified using photothermal deflection spectroscopy. A $\text{Cu}_3\text{N}/\text{ZnS}$ heterojunction diode with good current-voltage rectification behavior has been demonstrated experimentally, but no photocurrent is generated under illumination. The absence of photocurrent can be explained by a large concentration of Cu_i recombination centers capturing electrons in p -type Cu_3N .

DOI: [10.1103/PhysRevB.97.245201](https://doi.org/10.1103/PhysRevB.97.245201)

I. INTRODUCTION

Thin-film photovoltaic materials are predominantly made of defect-tolerant semiconductors like $\text{Cu}(\text{In,Ga})\text{Se}_2$ and CdTe . The use of low-cost materials deposition techniques produces polycrystalline thin films with numerous crystallographic imperfections like point defects and grain boundaries. In spite of such defects, $\text{Cu}(\text{In,Ga})\text{Se}_2$ and CdTe are capable of achieving high solar cell efficiencies in excess of 20%. This is in contrast with semiconductors like GaAs or InP , which typically require high-cost epitaxial thin-film deposition methods on single-crystal substrates for high solar cell efficiencies. $\text{Cu}_2\text{ZnSn}(\text{S,Se})_4$ has recently emerged as a promising solar energy conversion material comprising earth-abundant elements, and can be deposited using low-cost methods like that used for $\text{Cu}(\text{In,Ga})\text{Se}_2$ and CdTe . However, the record $\text{Cu}_2\text{ZnSn}(\text{S,Se})_4$ solar cell efficiency is 12.7% [1], significantly lower than the best solar cell efficiencies obtained for $\text{Cu}(\text{In,Ga})\text{Se}_2$ and CdTe . Recent first-principles calculations [2] on the intrinsic point defects in $\text{Cu}_2\text{ZnSn}(\text{S,Se})_4$ have shown that the Sn_{Cu} and Sn_{Zn} antisite defects are recombination centers with deep defect transition levels, limiting the open-circuit voltage values of $\text{Cu}_2\text{ZnSn}(\text{S,Se})_4$ solar cells. Ideally, the search for a candidate solar energy conversion material should consider the elemental abundance of the material, its tolerance to crystallographic imperfections like point defects and grain boundaries, and its optical absorption coefficient.

Cu_3N has been proposed as a defect-tolerant, earth-abundant semiconductor for solar energy conversion by Zakutayev *et al.* [3], who reported an optical absorption onset of 1.4 eV for Cu_3N despite its calculated indirect fundamental band gap of 1.0 eV. Zakutayev and co-workers speculated that semiconductors for which the valence band maximum is dominated by antibonding states are likely to have shallow defect states within the band gap. This applies for Cu_3N but does

not hold for conventional III-V semiconductors like GaAs , for which the valence band and the conduction band mainly comprise bonding states and antibonding states, respectively. This speculation about defect tolerance is in accord with prior theoretical studies of CuInSe_2 , in which the hybridization of $\text{Cu } d$ orbitals and $\text{Se } p$ orbitals results in both bonding and antibonding states in the valence band maximum [4,5]. The antibonding states due to p - d repulsion push the valence band maximum up in chalcopyrite (I-III-VI₂) CuInSe_2 , resulting in an anomalously small band gap and high valence band maximum (relative to the vacuum level) compared to the binary II-VI analogs like ZnSe or CdSe . Copper vacancies in CuInSe_2 thus have a very shallow acceptor level with respect to the valence band maximum, with defect-state eigenvalues that are resonant within the valence band [6]. While this is a general guideline to predict semiconductors with shallow defect levels in the band gap that are attributed to specific point defects (like copper vacancies in CuInSe_2), it is essential that all possible point defects are considered when evaluating materials for solar energy conversion, since some of them could act as recombination centers or carrier traps, undermining solar cell performance.

There have been several prior density functional theory studies of Cu_3N in which the indirect band gap values of Cu_3N were significantly underestimated as 0.5 eV [7] and 0.23 eV [8], using the generalized-gradient approximation (GGA) and local-density approximation (LDA), respectively. A reasonable indirect band gap value of 1.0 eV was obtained by Zakutayev *et al.* [3] when combining the GGA functional with an additional on-site Coulomb interaction term $U_d(\text{Cu}) = 5$ eV and GW quasiparticle energy calculations. This underestimation in band gaps can lead to large uncertainties in the positions of defect charge-state transition levels that lie within the band gap. In this study, we employed the Heyd, Scuseria, and

Ernzerhof (HSE06) exchange-correlation functional [9,10], which can accurately describe the band gap and electronic structure of semiconductors and insulators [11]. HSE06 is also expected to partially correct for the self-interaction errors for localized d electrons [12], which is especially helpful for copper-containing compounds like Cu_3N . We can therefore acquire a comprehensive understanding of the intrinsic point defects in Cu_3N by using the screened-exchange hybrid density functional HSE06.

Cu_3N is a metastable semiconductor that undergoes spontaneous thermal decomposition into Cu metal and N_2 gas when heated to temperatures exceeding 200°C in vacuum [13,14]. Experimentally, Cu_3N has been synthesized by a variety of techniques, including radio frequency (rf) reactive magnetron sputtering [3,15,16] and molecular beam epitaxy [17,18]. Controlled bipolar doping of Cu_3N has been demonstrated by varying the thin-film deposition conditions [3,17,19]. Copper-poor growth conditions result in the formation of p -type films, while copper-rich growth conditions yield n -type films. Despite its indirect band gap, high absorption coefficient values have also been reported in Cu_3N [3,17], making it a potentially interesting semiconductor for thin-film photovoltaic applications. To complement our predictions from density functional theory, we have also synthesized Cu_3N thin films by reactive magnetron sputtering and characterized them extensively in this study.

II. METHODS

A. Computational details

The screened-exchange hybrid density functional HSE06 as implemented in the Vienna *ab initio* simulation package (VASP) [20] was used for all calculations in this study. 25% of the short-range exchange interaction of the Perdew-Burke-Ernzerhof (PBE) [21] generalized-gradient approximation is replaced by the short-range nonlocal Hartree-Fock (HF) exchange interaction in the HSE06 functional. For this study, an exchange-screening parameter ω of 0.2 \AA^{-1} was applied. All calculations were performed using the projector augmented wave (PAW) method [22]. Cutoff energies were set to 400 eV for all calculations. In this study, Cu ($3d$, $4s$) and N ($2s$, $2p$) were used as valence electron states. Calculations of the band structure, density of states, and dielectric function were performed using the 4-atom primitive unit cell with $10 \times 10 \times 10$ Γ -centered k -point grids. The frequency-dependent dielectric function was calculated using the projector-augmented wave (PAW) method described in detail in [23] and the independent-particle approximation (IPA), considering only direct transitions between occupied and empty states. A dense $16 \times 16 \times 16$ Γ -centered k -point mesh was used to calculate the dielectric function for the 4-atom primitive unit cell.

The intrinsic point defects examined in this study include vacancies, antisite defects, and interstitial defects in the host Cu_3N crystal. For these calculations, $2 \times 2 \times 2$ Γ -centered k -point grids were used for $3 \times 3 \times 3$ (108-atom) supercells, and spin polarization was enabled. The perfect defect-free crystal was first fully optimized for the lattice constants and internal ionic coordinates until the residual forces were less than 0.01 eV/\AA . These optimized lattice constants were

then fixed for supercells containing point defects, and the ions were fully relaxed until residual forces were less than 0.01 eV/\AA . For further analysis of the copper interstitial Cu_i defect in Sec. III C, calculations of the density of states and partial charge densities were done using $4 \times 4 \times 4$ (256-atom) supercells with $2 \times 2 \times 2$ Γ -centered k -point grids to confirm that there are no erroneous electrostatic interactions between point defects in periodic $3 \times 3 \times 3$ supercells.

The formation energies of intrinsic point defects are calculated as [2,24–26]

$$\Delta H_f[D, q] = E[D, q] - E_{\text{host}} + \sum n_i \mu_i + q(E_{\text{VBM}} + E_F), \quad (1)$$

where $E[D, q]$ is the total energy of the supercell with a defect D in charge state q , corrected with the Makov-Payne image charge correction scheme that accounts for spurious electrostatic interactions between charged defects in periodic supercells. This image charge correction scheme is described in further detail in Sec. 1 of the Appendix, and a theoretical dielectric constant of 7.51 derived from the dielectric function calculated in Sec. III A was used for the image charge corrections. E_{host} is the total energy of the defect-free supercell. n_i is the number of atoms transferred from the supercell to the chemical reservoir of element i ; $n_i = 1$ if an atom is removed and $n_i = -1$ if an atom is added. μ_i refers to the chemical potential of atom i and represents the strength of the chemical reservoir; the formation energy of a vacancy of atom i is high when μ_i is high. E_{VBM} refers to the energy of the valence band maximum (VBM) and E_F represents the Fermi level measured from the VBM, which can vary within the band gap of the material between E_{VBM} and E_{CBM} , where E_{CBM} refers to the energy of the conduction band minimum (CBM).

The Fermi energy where the charge state of a point defect D changes from q to q' is defined as the charge-state transition level. Derived from Eq. (1), the following expression can be used to calculate the charge-state transition level [2,26]:

$$\varepsilon[D, q/q'] = (E[D, q] - E[D, q']) / (q' - q) - E_{\text{VBM}}. \quad (2)$$

For calculations of the surface energies of Cu_3N , the (001), (110), and (111) surfaces were selected since these are the most commonly studied surfaces in cubic crystal structures. We have used computational supercells comprising a slab of Cu_3N approximately 10 \AA thick followed by a vacuum layer approximately 20 \AA thick for all three surfaces. The crystal slabs have thicknesses of six planes (three formula units), eight planes (four formula units), and 12 planes (12 formula units) for the (001), (110), and (111) surfaces, respectively. For each crystal orientation, we have calculated the surface energies for (i) the defect-free crystal slab in which the surface atoms do not form or break new bonds, and (ii) crystal slabs in which Cu and/or N atoms are added to the surface to give Cu-terminated, N-terminated, or mixed cation- and anion-terminated surfaces. The optimized HSE06 lattice constants were used for the supercells in-plane of the crystal slabs, and all ions were fully relaxed until residual forces were less than 0.01 eV/\AA .

The surface energy of the crystal surface $\Delta H_{\text{surface}}$ can be calculated using the following expression [27]:

$$\Delta H_{\text{surface}} = (E_{\text{surface}} - NE_{\text{host}} + \sum n_i \mu_i) / 2A, \quad (3)$$

where E_{surface} is the total energy of the supercell containing the crystal slab and the vacuum layer, NE_{host} is the energy of an equivalent number of atoms in the bulk or host crystal in the absence of a surface, n_i is the number of atoms added to the surface from the chemical reservoir of element i to give various surface terminations, μ_i refers to the chemical potential of atom i , and A is the surface area of the crystal slab. For these surface energy calculations, we set the chemical potentials of Cu and N to their standard-state values μ_i^0 .

B. Thin-film deposition and characterization

Cu_3N thin-film samples were deposited using radio frequency (rf) reactive magnetron sputtering from a 2-in. copper target on soda-lime glass substrates at a temperature of 160 °C and rf power of 25 W. The total pressure was maintained at 20.0 mTorr with 20 sccm flow rate of N_2 (99.999% purity). The 100% N_2 partial pressure gives copper-poor, nitrogen-rich growth conditions that yield p -type films. To fabricate the p - n junction, a 1- μm -thick molybdenum film was sputtered as the back contact on soda-lime glass substrates. Next, 350 nm of Cu_3N was deposited on the molybdenum back contact using rf sputtering at 25 W at 160 °C substrate temperature, with 20.0 mTorr sputtering pressure and 20 sccm N_2 flow rate. This was followed by a ZnS n -type buffer layer deposited using atomic layer deposition (ALD) at 125 °C, using diethylzinc as the Zn precursor and H_2S as the S precursor [28]. The employed ALD pulse cycle was diethylzinc – N_2 purge – H_2S – N_2 purge for 1-30-0.25-30 s, respectively. Five hundred cycles of ALD were used to grow the ZnS film at approximately 1 Å/cycle. The H_2S gas was formed by thermal decomposition of thioacetamide at 115 °C. Next, 250 nm of aluminum-doped zinc oxide (Al:ZnO) was deposited as the transparent top electrode, followed by aluminum metal fingers 3 μm thick sputtered through a shadow mask. The final device area of 0.45 cm^2 was defined by scribing through the soft Cu_3N films to expose the Mo back contact. Indium dots were soldered onto the Mo back contact as Ohmic electrical contacts. All film thicknesses were measured using cross-section scanning electron microscopy (SEM). To ascertain the suitability of Mo as an Ohmic contact for Cu_3N , we have tested Mo and In contacts on Cu_3N thin films deposited on soda-lime glass substrates, using the Cu_3N deposition conditions described above. Mo contacts were deposited using DC sputtering on the Cu_3N samples through a shadow mask, while In contacts were soldered directly onto the Cu_3N film surface.

Photothermal deflection spectroscopy (PDS) measurements were performed using a home-built setup described by Vandewal *et al.* [29]. A mechanically chopped (3.333 Hz) monochromatic light source with 5-nm spectral resolution using a 100-W halogen pump lamp was focused on the sample. The sample was immersed in degassed and filtered perfluorohexane (C6F14, 3M Fluorinert FC-72), which serves as the deflection medium. Ultraviolet-visible spectroscopy (UV-Vis) measurements were performed using a Cary 6000i

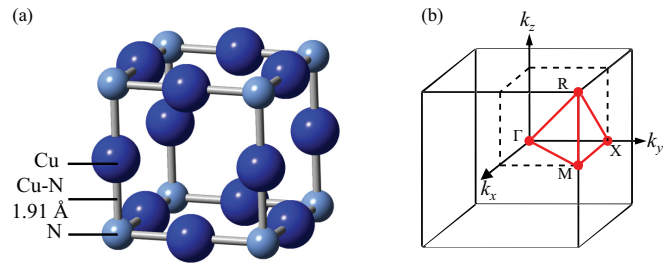


FIG. 1. (a) Primitive 4-atom unit cell for cubic Cu_3N . The crystal structure basis consists of one nitrogen atom at fractional coordinates $(0, 0, 0)$ and three copper atoms at fractional coordinates $(\frac{1}{2}, 0, 0)$, $(0, \frac{1}{2}, 0)$ and $(0, 0, \frac{1}{2})$. (b) First Brillouin zone of Cu_3N , with the high-symmetry points Γ $(0, 0, 0)$, M $(\frac{\pi}{a}, \frac{\pi}{a}, 0)$, R $(\frac{\pi}{a}, \frac{\pi}{a}, \frac{\pi}{a})$, and X $(\frac{\pi}{a}, 0, 0)$ labeled and joined by red lines.

UV/Vis/NIR spectrometer (Agilent Technologies, Inc.). Photoelectron spectroscopy in air (PESA) measurements were done with a Riken AC-2 Photoelectron Spectrometer (Riken Keiki Co. Ltd., Japan) equipped with an ultraviolet (UV) source. For Hall effect measurements, a standard six-probe method was used: two for the current source, two for the longitudinal voltage electrodes (parallel to the direction of current flow), and two for the Hall voltage electrodes (perpendicular to the direction of current flow). Electrical contacts were made to the sample using gold wires and silver paint, and the sample was placed in a helium cryostat (Physical Property Measurement System, Quantum Design, Inc.). Hall effect measurements were performed using a superconducting magnet with the magnetic field ranging between -8×10^4 and 8×10^4 Gauss, applied vertically to the sample surface.

III. RESULTS FROM FIRST-PRINCIPLES CALCULATIONS

A. Fundamental properties of Cu_3N

The crystal structure of Cu_3N is cubic [Fig. 1(a)], with space group symmetry $Pm-3m$ (space group no. 221). It is also known as the anti- ReO_3 (anti-rhenium trioxide) structure, which is similar to the perovskite structure (chemical formula ABX_3) except that the atom at the center of the cubic crystal structure is removed, and the cation and anion positions are exchanged. The atoms forming the basis of the primitive unit cell are one nitrogen atom at fractional coordinates $(0, 0, 0)$ [Wyckoff site $1a$] and three copper atoms at fractional coordinates $(\frac{1}{2}, 0, 0)$, $(0, \frac{1}{2}, 0)$, and $(0, 0, \frac{1}{2})$ [Wyckoff site $3d$]. Figure 1(b) is a schematic representation of the first Brillouin zone of the Cu_3N crystal, with the high-symmetry points Γ , M , R , and X labeled and joined by red lines. The calculated HSE06 lattice constant a for Cu_3N is 3.81 Å, and the Cu-N bond length is 1.91 Å.

The HSE06 band structure of Cu_3N is shown in Fig. 2(a), plotted along the high-symmetry directions M $(\frac{\pi}{a}, \frac{\pi}{a}, 0)$, Γ $(0, 0, 0)$, X $(\frac{\pi}{a}, 0, 0)$, M $(\frac{\pi}{a}, \frac{\pi}{a}, 0)$, R $(\frac{\pi}{a}, \frac{\pi}{a}, \frac{\pi}{a})$ and Γ $(0, 0, 0)$. Spin-orbit coupling has been included in the band structure calculations. Cu_3N has a fundamental indirect transition of 0.95 eV from the VBM at the R point to the CBM at the M point. The direct transitions at the M and R points are 1.89 and 1.82 eV, respectively, giving a direct band gap of

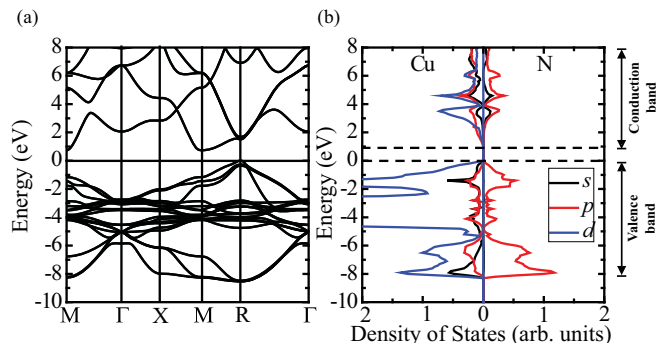


FIG. 2. (a) Electronic band structure of Cu_3N calculated using the HSE06 functional and (b) atomic- and orbital-resolved density of states plot of Cu_3N .

1.82 eV. The calculated band structure is in close agreement with the band structure calculated using *GW* quasiparticle energy calculations in [3], in which the indirect transition is 1.0 eV and the direct transition is 1.6 eV. It also shows similar curvatures but more accurate band gap values compared to the LDA band structure of Cu_3N published in [8]. The bands near the extrema of both the VBM and CBM show comparable dispersions, indicative of similar carrier effective masses at those bands.

The total density of states (DOS) of Cu_3N [Fig. 2(b)] was calculated using the tetrahedron method with Blöchl corrections [30]. The upper valence band predominantly comprises the hybridization between Cu-3*d* and N-2*p* orbitals, suggesting that *p-d* repulsion is giving rise to antibonding states near the VBM, similar to that in CuInSe_2 . In Cu_3N , there is also a strong contribution to the conduction band states from the Cu-3*p* and Cu-3*d* orbitals, different from the conduction band states in CuInSe_2 which predominantly comprise In-5*s* and Se-4*p* orbitals [2].

The thermodynamic stability of Cu_3N with respect to its constituent elements Cu and N in their ground states was calculated using the HSE06 functional. The formation energies were calculated at $T = 0$ K and zero point motion has been neglected. Elemental Cu metal (space group symmetry *Fm-3m*) and the nitrogen molecule (N_2) were used in these calculations, and the calculated HSE06 chemical potentials μ_i^0 are -3.07 eV/atom and -4.76 eV/atom for Cu and N in their standard states, respectively. The cohesive energy of Cu_3N is -3.32 eV/atom in Cu_3N with respect to individual Cu and N atoms, and its formation energy ΔH_f is $+0.18$ eV/atom with respect to elemental Cu metal and the N_2 molecule. These values match the results reported in [31] for the cohesive energy of -3.6 eV/atom and formation energy ΔH_f of $+0.2$ eV/atom. The results indicate that in thermodynamic equilibrium, Cu_3N is a metastable semiconductor that preferentially decomposes into metallic Cu and N_2 gas at high temperatures in vacuum. However, it is possible to synthesize Cu_3N in processes that operate under nonequilibrium conditions like reactive magnetron sputtering. The relatively strong cohesive energy of -3.32 eV/atom is comparable to that of other semiconductors like GaAs (-3.26 eV/atom) and GaN (-4.48 eV/atom) [32], suggesting that Cu_3N is metastable with respect to its constituent elements not because of weak

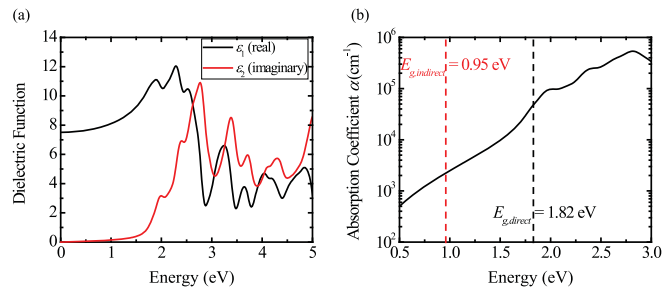


FIG. 3. (a) The complex dielectric function $\varepsilon(\omega) = \varepsilon_1(\omega) + i\varepsilon_2(\omega)$ of Cu_3N , where $\varepsilon_1(\omega)$ is the real part (black line) and $\varepsilon_2(\omega)$ is the imaginary part (red line) of the dielectric function. (b) Absorption coefficient values α of Cu_3N as a function of photon energy, derived from the complex dielectric function.

chemical bonding but due to the strong triple bond in the N_2 molecule.

Defining the relative chemical potentials $\Delta\mu_i$ as the chemical potential of element i with respect to its standard state ($\Delta\mu_i = \mu_i - \mu_i^0$), $\Delta\mu_i$ of the constituents Cu and N have to sum up to the formation energy of the host compound Cu_3N in thermodynamic equilibrium ($+0.72$ eV/formula unit):

$$3\Delta\mu_{\text{Cu}} + \Delta\mu_{\text{N}} = \Delta H_f(\text{Cu}_3\text{N}). \quad (4)$$

Since Cu_3N is a metastable compound, there is no range of chemical potentials under which the compound is thermodynamically stable. Under experimental conditions, however, thin-film deposition techniques like sputter deposition do not pertain to thermodynamic equilibrium. In this study, we will investigate defect properties in Cu_3N with elemental chemical potentials corresponding to (i) copper-poor growth conditions ($\Delta\mu_{\text{Cu}} = -0.64$ eV, $\Delta\mu_{\text{N}} = +2.64$ eV), and (ii) copper-rich growth conditions ($\Delta\mu_{\text{Cu}} = 0$ eV, $\Delta\mu_{\text{N}} = +0.72$ eV), satisfying Eq. (4). Under these conditions, copper metal cannot precipitate, i.e., $\Delta\mu_{\text{Cu}} \leq 0$ eV. From Eq. (1), formation energies of point defects depend on $\Delta\mu_i$ of the constituent elements, and since $\Delta\mu_i$ is directly controlled by experimental growth conditions, defect formation energies and defect concentrations can also be controlled.

The complex dielectric function describes the polarization response of a material to an externally applied electric field [33]. It can be expressed as $\varepsilon(\omega) = \varepsilon_1(\omega) + i\varepsilon_2(\omega) = (n + i\kappa)^2$, where $\varepsilon_1(\omega)$ and $\varepsilon_2(\omega)$ are the real and imaginary parts of the complex dielectric function, respectively; n is the refractive index; and κ is the extinction coefficient of Cu_3N . The complex dielectric function of Cu_3N calculated using the HSE06 functional in the independent-particle approximation (IPA) is given in Fig. 3(a). The absorption coefficient values α derived from the dielectric function, calculated as $\alpha = 4\pi\kappa/\lambda$ where λ is the photon excitation wavelength, are plotted as a function of photon energy in Fig. 3(b).

The static, zero-frequency relative permittivity (static dielectric constant) is given by the real part of the complex dielectric function $\varepsilon_1(\omega)$ at zero energy. From Fig. 3(a), the static dielectric constant of Cu_3N is 7.51, which was used for the Makov-Payne image charge corrections in the total energy calculations for point defects [Sec. III B]. The onset of the imaginary part $\varepsilon_2(\omega)$ of the complex dielectric function

reflects the band gap energy at which photon absorption begins [34], and this occurs at the minimum direct band gap since only direct band-to-band transitions are considered, neglecting phonon-assisted absorption. From Fig. 3(a), there is a strong onset in $\varepsilon_2(\omega)$ at around 1.8 eV, corresponding to the direct optical transitions at the M and R points in the first Brillouin zone. Above 1.8 eV, relatively high absorption coefficient values of between 10^4 and 10^6 cm^{-1} are observed, typical of direct band-to-band optical transitions. From Fig. 3(b), the peak in absorption coefficient at around 2.8 eV is consistent with that observed in the absorption coefficient spectrum measured using spectroscopic ellipsometry in [35]. Although only direct transitions are considered in this calculation, nonzero values of $\varepsilon_2(\omega)$ are observed between 0 and 1.8 eV, due to the fact that density functional theory calculations are only theoretical approximations to actual materials. This gives rise to the gradual increase in absorption coefficient values below the direct band gap of 1.82 eV [Fig. 3(b)]. The gradual optical absorption tail below the direct band gap has also been observed in a similar HSE06 dielectric function calculation of Cu_3N [35], and in other dielectric function calculations based on hybrid functionals [36]. While other first-principles methods like the GW [37] can provide better approximations of the optical properties of Cu_3N , they require significantly greater computational expense and are beyond the scope of this paper.

B. Point defect formation energies and transition levels

The native point defects in Cu_3N investigated in this study are the vacancies (V_{Cu} , V_{N}), antisite defects (Cu_{N} , N_{Cu}), and interstitials (Cu_{i} , N_{i}). V_X refers to a vacancy at site X , X_Y refers to an atom X occupying site Y , and X_{i} refers to an interstitial of atom X located at the center of the cubic crystal structure. These defects are classified as acceptors or donors depending on the valences of the elements—the formal charges for the elements are Cu^{1+} and N^{3-} in the defect-free Cu_3N crystal. Thus, V_{Cu} , N_{Cu} , and N_{i} can behave as acceptors, while V_{N} , Cu_{N} , and Cu_{i} can act as donors.

Using Eq. (1), the calculated intrinsic point defect formation energies ΔH_f for Cu_3N as a function of Fermi energy are plotted in Fig. 4(a) for copper-poor growth conditions ($\Delta\mu_{\text{Cu}} = -0.64$ eV, $\Delta\mu_{\text{N}} = +2.64$ eV) and Fig. 4(b) for copper-rich growth conditions ($\Delta\mu_{\text{Cu}} = 0$ eV, $\Delta\mu_{\text{N}} = +0.72$ eV). We have also calculated the equilibrium Fermi levels (E_F) at 300 K (details given in Sec. 2 of the Appendix) for both copper-poor and copper-rich growth conditions; they are indicated by vertical dashed lines in Fig. 4. From Fig. 4, there are only two native point defects with formation energies of approximately 1.0 eV or less across all Fermi levels within the band gap, namely, V_{Cu} and Cu_{i} . V_{Cu} and Cu_{i} are thus the point defects with the highest concentrations in the material and are likely to dominate the bulk electrical properties of Cu_3N . The actual concentrations of these point defects depend on the chemical potentials of the constituent elements μ_i during growth. From Eq. (1), copper-poor growth conditions (low $\Delta\mu_{\text{Cu}}$ or high $\Delta\mu_{\text{N}}$) favor the formation of V_{Cu} [Fig. 4(a)], while copper-rich growth conditions (low $\Delta\mu_{\text{N}}$ or high $\Delta\mu_{\text{Cu}}$) favor the formation of Cu_{i} [Fig. 4(b)]. These results are in good agreement with the calculations by Fioretti *et al.* [19], reporting

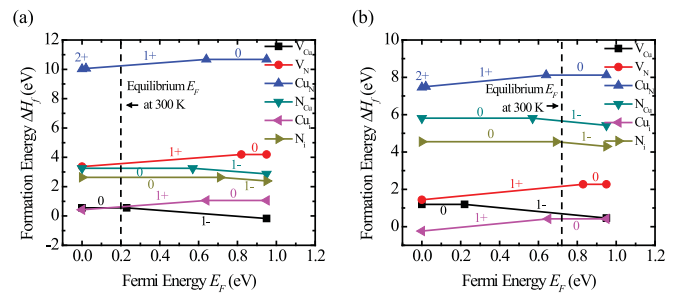


FIG. 4. Defect formation energies in Cu_3N as a function of Fermi energy under (a) copper-poor growth conditions ($\Delta\mu_{\text{Cu}} = -0.64$ eV, $\Delta\mu_{\text{N}} = +2.64$ eV) and (b) copper-rich growth conditions ($\Delta\mu_{\text{Cu}} = 0$ eV, $\Delta\mu_{\text{N}} = +0.72$ eV). The various defect charge states are labeled, and the charge-state transition levels are given as points connecting the lines representing different charge states. The equilibrium Fermi level (E_F) at 300 K is given by the vertical dashed lines.

V_{Cu} and Cu_{i} as the dominant point defects. In the experimental section of this study (Sec. IV), we employ copper-poor growth conditions to obtain weak p -type doping in our Cu_3N films.

The calculated equilibrium Fermi level at 300 K is 0.20 eV under copper-poor growth conditions [Fig. 4(a)] and 0.72 eV under copper-rich growth conditions [Fig. 4(b)]. Over this range of Fermi levels, overall charge neutrality is predominantly maintained by a balance between the V_{Cu}^{1-} and $\text{Cu}_{\text{i}}^{1+}$ charge states in Cu_3N . This is in accord with the assertion in [19] that Cu_3N is a heavily compensated semiconductor. Calculations of the charge-neutral ($V_{\text{Cu}} + \text{Cu}_{\text{i}})^0$ Frenkel pair have also been done, indicating defect formation energies of 0.91 eV when V_{Cu} is adjacent to Cu_{i} (separated by 2.69 Å), and 1.11 eV when V_{Cu} and Cu_{i} are separated by 8.93 Å. These defect formation energies are in between that of the individual V_{Cu} and Cu_{i} defects. The other four native point defects (V_{N} , Cu_{N} , N_{Cu} , and N_{i}) have formation energies above 1.0 eV and thus only negligibly small concentrations of these defects will form. Among these, the antisite defects Cu_{N} and N_{Cu} have especially high formation energies above 3.0 eV, likely due to the very large difference in electronegativity between the two elements Cu and N. Switching the positions of both elements in the Cu_3N crystal lattice will induce high Coulomb repulsion within the Cu_3N crystal lattice, rendering the antisite defect highly unstable.

Using Eq. (2), we have also calculated the defect charge-state transition levels $\varepsilon[D, q/q']$, and the point defects with charge-state transition levels lying within the band gap are shown in Fig. 5. V_{Cu} is a shallow acceptor with a $(0/-)$ transition level 0.23 eV above the VBM. Due to its shallow defect transition level, it is the predominant acceptor defect in p -type films. Its defect transition level is an excellent match for the acceptor ionization activation energy E_A of 0.20 eV from temperature-dependent Hall effect data in [19]. This indicates that the Makov-Payne image charge correction employed in this study yields reasonable results, while the acceptor level E_A of 0.12 eV calculated without any corrections for self-interacting errors in [19] underestimates the acceptor ionization energy. Cu_{i} has a relatively deep $(0/+)$ defect transition level of 0.64 eV above the VBM (0.31 eV below the CBM)

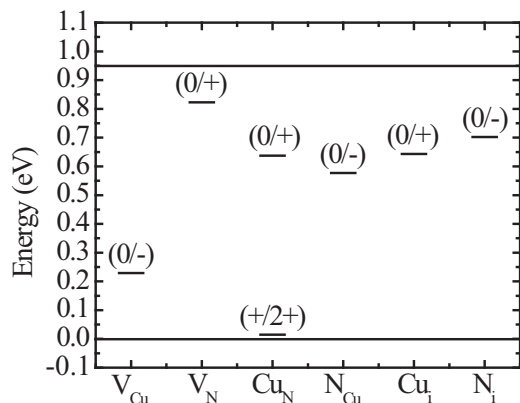


FIG. 5. Point defect charge-state transition levels $\varepsilon[D,q/q']$ in Cu_3N . Only point defects with charge-state transition levels lying within the band gap of Cu_3N are shown. The same defect transition levels can be visualized in Fig. 4 as points connecting the lines representing different charge states.

and is the dominant donor-type defect given its significantly higher concentration compared to V_N . In p -type films, the Fermi level is close to the VBM and Cu_i will be ionized in the $1+$ charge state, rendering it attractive to electrons (minority carriers). Considering the very low formation energy of the Cu_i defect [Fig. 4], its large concentration can result in substantial capture of electrons in p -type films. After capturing an electron, the charge state of Cu_i changes from $+1$ to 0 . The resultant neutral charge state is not repulsive to majority carriers (holes), thus allowing significant Shockley-Read-Hall recombination. This property is especially detrimental in optoelectronic devices like solar cells which demand high minority carrier lifetimes for high open-circuit voltages, since device efficiency degrades significantly if minority carriers are captured at point defects. V_N has a $(0/+)$ donor level 0.13 eV below the CBM, while N_i has a deep $(0/-)$ acceptor level 0.70 eV above the VBM. Due to the relatively high formation energies of V_N and N_i , they are unlikely to influence bulk electrical properties. The other two point defects, Cu_N and N_{Cu} , have deep transition levels near midgap [0.64 eV above the VBM for the Cu_N $(0/+)$ state and 0.58 eV above the VBM for the N_{Cu} $(0/-)$ state], but they will have no impact on bulk electrical properties due to their negligibly small concentrations. Overall, these results are in close agreement with the findings in [3,19]. However, we emphasize that the impact of Cu_i can be more detrimental than previously reported by other studies, given its very low formation energy and deep $(0/+)$ transition level.

C. Analysis of Cu_i defect

To further elucidate the characteristics of the charge-neutral Cu_i^0 defect and its role in carrier transport and recombination, the total density of states for the Cu_i^0 defect in a 256-atom Cu_3N host crystal is compared with that of the defect-free host crystal in Fig. 6. We observe an additional continuum of defect states extending from 0.5 eV above the VBM up to the CBM for the Cu_i^0 defect in Cu_3N . Since these defect states are formed in the upper part of the band gap essentially overlapping

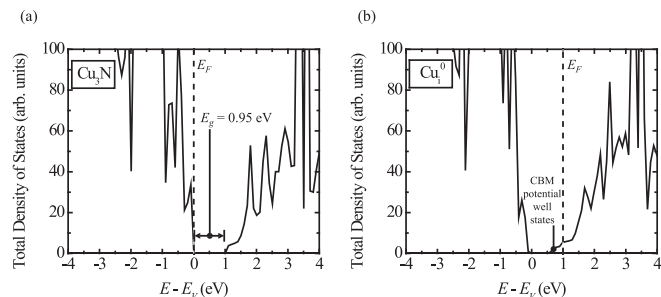


FIG. 6. Total density of states for (a) 256-atom Cu_3N host crystal, and (b) Cu_i^0 defect in 256-atom Cu_3N host crystal. The VBM has been referenced to 0 eV in energy. Calculated Fermi levels are given by vertical dashed lines.

with the CBM, these sub-band-gap defect states behave as conduction band potential wells approximately 0.45 eV in depth, in agreement with the calculated $(0/+)$ defect transition level of 0.31 eV below the CBM for the Cu_i defect.

Figure 7(a) shows the partial electronic charge density distribution for the sub-band-gap continuum of defect states for the Cu_i^0 defect in the 256-atom Cu_3N host crystal along the (001) plane, calculated by integrating the density of states from the VBM up to the Fermi level shown in Fig. 6(b). The states induced by the Cu_i^0 defect show localized character as described by the high partial charge densities around the defect. Figure 7(b) is a comparison between the partial density of states for (i) a copper interstitial, and (ii) a copper atom located far from the interstitial defect approximating bulklike behavior in the 256-atom Cu_3N host crystal. For the Cu_i^0 defect, a strong contribution to the sub-band-gap continuum of states from 0.5 eV above the VBM up to the CBM is observed, confirming that the sub-band-gap partial charge densities are largely localized on the Cu_i^0 defect. An analysis of the orbital-resolved density of states shows that this sub-band-gap continuum of defect states is predominantly from the Cu - $4s$ states of the Cu_i^0 defect, different in character from the Cu - $3p$ and Cu - $3d$ states that comprise the CBM.

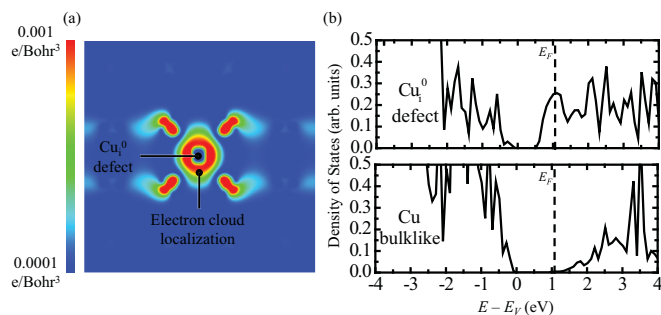


FIG. 7. (a) Partial electronic charge density distribution for the sub-band-gap continuum of states from the Cu_i^0 defect along the (001) plane in the 256-atom Cu_3N host crystal, calculated by integrating the density of states in Fig. 6(b) from the VBM to the Fermi level. (b) Partial density of states for the copper interstitial Cu_i^0 defect and a copper atom far from the defect with bulklike behavior in the 256-atom Cu_3N host crystal. The VBM has been referenced to 0 eV in energy. Calculated Fermi levels are given by vertical dashed lines.

TABLE I. Self-consistently calculated defect concentrations in Cu_3N (i) under copper-poor growth conditions ($\Delta\mu_{\text{Cu}} = -0.64$ eV, $\Delta\mu_{\text{N}} = +2.64$ eV) at 433 K with E_F at 0.25 eV, and (ii) copper-rich growth conditions ($\Delta\mu_{\text{Cu}} = 0$ eV, $\Delta\mu_{\text{N}} = +0.72$ eV) at 433 K with E_F at 0.69 eV. Defect concentrations below 10^0 cm^{-3} are labeled “Negligible.” $(V_{\text{Cu}} + \text{Cu}_i)^0$ (near) and $(V_{\text{Cu}} + \text{Cu}_i)^0$ (far) refer to the $(V_{\text{Cu}} + \text{Cu}_i)$ charge-neutral Frenkel pair defects separated by 2.69 and 8.93 Å, respectively.

Defect	$C[D,q]$ (cm^{-3}) (copper-poor)	$C[D,q]$ (cm^{-3}) (copper-rich)
V_{Cu}^0	2.33×10^{16}	8.41×10^8
V_{Cu}^-	4.07×10^{16}	1.92×10^{14}
V_{N}^0	Negligible	Negligible
V_{N}^+	Negligible	Negligible
Cu_{N}^0	Negligible	Negligible
Cu_{N}^+	Negligible	Negligible
$\text{Cu}_{\text{N}}^{2+}$	Negligible	Negligible
N_{Cu}^0	Negligible	Negligible
N_{Cu}^-	Negligible	Negligible
Cu_i^0	8.95×10^9	2.48×10^{17}
Cu_i^+	3.35×10^{14}	7.08×10^{16}
N_i^0	Negligible	Negligible
N_i^-	Negligible	Negligible
$(V_{\text{Cu}} + \text{Cu}_i)^0$ (near)	4.17×10^{11}	4.17×10^{11}
$(V_{\text{Cu}} + \text{Cu}_i)^0$ (far)	2.15×10^9	2.15×10^9

The conduction band potential well depth of 0.45 eV is sufficiently large to confine electrons at Cu_i defects with low probability of reexcitation back to the conduction band. In p -type Cu_3N films, Cu_i defects exist in the $1+$ charge state [Fig. 4(a)] and are highly attractive to electrons (minority carriers). Thus, these Cu_i potential wells are also strong mediators of Shockley-Read-Hall recombination in p -type Cu_3N .

D. Estimation of defect concentrations

Following the methodology described in Sec. 2 of the Appendix, we have self-consistently determined E_F , $C[D,q]$ and the free carrier concentrations p and n . The values of $m_{e,\text{DOS}}^*$ and $m_{h,\text{DOS}}^*$ are estimated to be $0.53 m_0$ and $0.47 m_0$, giving $N_C = 9.57 \times 10^{18} \text{ cm}^{-3}$ and $N_V = 8.11 \times 10^{18} \text{ cm}^{-3}$. The calculated defect concentrations at $T = 433$ K under copper-poor growth conditions ($\Delta\mu_{\text{Cu}} = -0.64$ eV, $\Delta\mu_{\text{N}} = +2.64$ eV) and copper-rich growth conditions ($\Delta\mu_{\text{Cu}} = 0$ eV, $\Delta\mu_{\text{N}} = +0.72$ eV) are presented in Table I. The self-consistently calculated E_F values at $T = 433$ K are 0.25 eV for copper-poor growth conditions and 0.69 eV for copper-rich growth conditions. Assuming that the defect concentrations at $T = 433$ K are frozen-in when quenched to 300 K, we can also calculate the equilibrium E_F at $T = 300$ K using the Fermi-Dirac distribution. Under copper-poor growth conditions, the calculated E_F value at 300 K is 0.20 eV, giving p -type Cu_3N with a hole concentration p of $3.14 \times 10^{15} \text{ cm}^{-3}$. With copper-rich growth conditions, we obtain n -type Cu_3N with an E_F value at 300 K of 0.72 eV and electron concentration n of $1.44 \times 10^{15} \text{ cm}^{-3}$.

From Table I, we find that for both copper-poor and copper-rich growth conditions, V_{Cu} and Cu_i have defect concentrations in the range of 10^{14} - 10^{17} cm^{-3} and are the dominant intrinsic point defects giving rise to p -type and n -type conductivity, respectively. Under copper-poor growth conditions, the concentration of Cu_i^+ is $3.35 \times 10^{14} \text{ cm}^{-3}$, which is significantly larger than the steady-state minority carrier concentration ($\sim 10^{12} \text{ cm}^{-3}$) in solar cells under standard 1-sun illumination intensity. This large concentration of Cu_i^+ can cause significant Shockley-Read-Hall recombination in p -type Cu_3N , quenching any photocurrent that is generated. We note that while these calculations pertain to thermodynamic equilibrium conditions and do not reflect experimental growth conditions, the defect concentrations presented in Table I can give us some insight on the dominant point defects present in Cu_3N and the dependence of defect concentrations on growth conditions. Experimentally measured defect concentrations can differ quantitatively with the values presented in Table I.

E. Surface energy calculations

To determine the relative stability of various crystal facets in Cu_3N , we have performed surface energy calculations of the (001), (110), and (111) crystal surfaces with various surface terminations as described in Sec. II A, and the results are shown in Table II. Among the various crystal orientations and terminations, the (001) crystal slab with mixed cation and anion terminations on both surfaces gives the lowest surface energy of $70.87 \text{ meV}/\text{Å}^2$, indicating that it is thermodynamically favorable for the (001) crystal slab to spontaneously have mixed cation and anion terminations on both surfaces. Indeed, polar semiconductor surfaces with an unequal number of cations and anions at the surfaces are not charge neutral and are generally more likely to undergo surface reconstruction for energetic stability [27]. The other crystal orientations and terminations calculated here have relatively higher surface energies and hence lower thermodynamic stabilities.

In order to demonstrate that it is favorable for Cu_i defects to be incorporated in the Cu_3N host crystal during thin-film growth and that Cu_i defects can exist in large concentrations, we have performed additional surface energy calculations of the (001) crystal slab with mixed cation and anion terminations on both surfaces—the most stable configuration. An extra Cu atom was placed at two different sites: (i) the Cu_i site just above the (001) surface, and (ii) the Cu_i site just below the (001) surface. The calculated surface energies are 112.45 and $71.01 \text{ meV}/\text{Å}^2$ for cases (i) and (ii), respectively. This suggests that it is energetically favorable for Cu_i to be incorporated in the bulk during thin-film growth, as opposed to freely diffusing on the surface.

IV. EXPERIMENTAL RESULTS

A. Optical absorption in Cu_3N

Photothermal deflection spectroscopy (PDS) [38] is an indirect absorption measurement technique with dramatically higher sensitivity than conventional absorption techniques like ultraviolet-visible spectroscopy (UV-Vis), and can be used for the detection of sub-band-gap defect states. It measures

TABLE II. Surface energies in $\text{meV}/\text{\AA}^2$ of the (001), (110), and (111) orientations with various surface terminations. The chemical potentials of Cu and N are set at their standard-state values μ_i^0 (-3.07 eV/atom for Cu and -4.76 eV/atom for N).

	Surface energies ($\text{meV}/\text{\AA}^2$)		
	(001) Surface	(110) Surface	(111) Surface
Defect-free	82.92 ^a	102.00 ^a	101.71 ^b
Cu-terminated (both surfaces)	123.94	123.54	97.72
N-terminated (both surfaces)	N.A. ^c	N.A. ^c	119.42
Mixed cation- and anion-terminated (both surfaces)	70.87	98.38	N.A. ^c

^aCu-terminated (top surface) and mixed cation- and anion-terminated (bottom surface).

^bCu-terminated (top surface) and N-terminated (bottom surface).

^cNot applicable.

the local heating of a sample by absorption of photons that do not result in direct band-to-band transitions, i.e., photons of sub-band-gap energies in the case of direct band gap semiconductors. PDS has been previously applied for the detection of surface defect states in single-crystalline GaAs wafers [39]. In this study, we have successfully employed PDS to ascertain the existence of sub-band-gap Cu_i defect states. Optical absorption data for Cu_3N was obtained by combining PDS data for photon energies below the direct band gap of Cu_3N (0.5–1.82 eV) and UV-Vis data for photon energies above the direct band gap of Cu_3N (1.82–3.0 eV), in accordance with the procedure described in [40]. Using the measured transmittance and reflectance values from UV-Vis and assuming the same reflection values at both the air/film interface and the film/substrate interface, absorption coefficient values α can be calculated as $\alpha = (1/t) \ln[(1-R)^2/T]$ where t is the film thickness, R is the reflectance, and T is the transmittance [41]. The optical absorption coefficient spectrum of a Cu_3N thin film (approximately 1.2 μm thick) is shown in Fig. 8.

The experimental optical absorption coefficient spectrum presented in Fig. 8 is in qualitative agreement with the calculated absorption coefficient spectrum [Fig. 3(b)], but the absorption coefficient values measured here are lower than

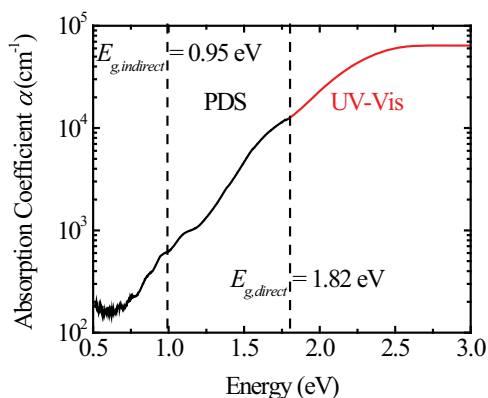


FIG. 8. Optical absorption coefficient spectrum of Cu_3N , obtained using a combination of photothermal deflection spectroscopy (PDS) for data points below 1.82 eV (direct band gap of Cu_3N) and ultraviolet-visible spectroscopy (UV-Vis) for data points above 1.82 eV.

predicted, most likely due to the assumption that no light is scattered. From Fig. 8, there is a distinct onset in optical absorption starting at energies around 0.65 eV up to the indirect band gap of 0.95 eV. This is in excellent agreement with the calculated Cu_i defect transition level of 0.64 eV above the VBM [Fig. 5] and the continuum of defect states starting from around 0.50 eV above the VBM in the density of states plot for the Cu_3N host crystal containing a Cu_i^0 defect [Fig. 6(b)]. We can thus attribute the experimental onset in optical absorption below the direct band gap of 1.82 eV to the presence of Cu_i point defects. Above 1.82 eV, the measured absorption coefficient is higher than 10^4 cm^{-1} , comparable to other direct band gap semiconductors like GaAs. While the measured absorption coefficient spectrum for Cu_3N in Fig. 8 is in overall agreement with that reported in [3,17,35], we emphasize that optical absorption below the direct bandgap of 1.82 eV is mediated by Cu_i defects and will not be present in the pristine defect-free Cu_3N crystal.

B. Carrier transport in Cu_3N

We performed Hall effect measurements on a 38-nm-thick Cu_3N sample as described in Sec. II B. The bulk resistivity was determined to be 13.2 $\Omega \text{ cm}$ at room temperature, with a hole concentration p of $1.78 \times 10^{17} \text{ cm}^{-3}$ and hole mobility μ_h of $2.65 \text{ cm}^2/(\text{V s})$. While the measured hole concentration of $1.78 \times 10^{17} \text{ cm}^{-3}$ is higher than the estimated value of $3.14 \times 10^{15} \text{ cm}^{-3}$ from Sec. III D, we have demonstrated that light p -type doping can be achieved using copper-poor growth conditions. The hole mobility of $2.65 \text{ cm}^2/(\text{V s})$ is relatively high considering the polycrystalline nature of Cu_3N and is comparable to hole mobility values of around $10 \text{ cm}^2/(\text{V s})$ for $\text{Cu}(\text{In,Ga})(\text{S,Se})_2$ in the literature [42].

Photoconductivity measurements were done on a 1.2- μm -thick Cu_3N sample under both 1-sun ($100 \text{ mW}/\text{cm}^2$) illumination and dark conditions, with indium Ohmic contacts soldered onto the Cu_3N films. The samples do not show strong photoconductivity response, with electrical conductivity doubling only after light-soaking for 1.5 h under 1-sun illumination. Since Cu_3N has a relatively high absorption coefficient of around 10^4 cm^{-1} at its direct band gap of 1.82 eV, the lack of photoconductivity points to fundamental limitations in the transport and collection of photogenerated carriers. Based on our theoretical predictions, we conclude that the

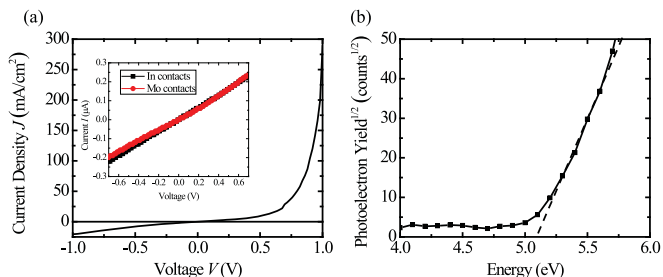


FIG. 9. (a) Current-voltage characteristics of a $\text{Cu}_3\text{N}/\text{ZnS}$ p - n junction without illumination. The inset of (a) shows linear current-voltage characteristics for both Mo and In contacts deposited on Cu_3N . (b) Photoelectron spectroscopy in air (PESA) measurement of a Cu_3N sample, giving an ionization potential value of 5.1 eV by extrapolating the photoelectron yield line down to the x axis.

lack of photoconductivity is due to the high concentration of Cu_i defects that behave as deep conduction band potential wells that easily capture photogenerated electrons and mediate Shockley-Read-Hall recombination.

C. Characteristics of $\text{Cu}_3\text{N}/\text{ZnS}$ p - n junction

To further examine the feasibility of Cu_3N as a photovoltaic absorber layer, we have fabricated a $\text{Cu}_3\text{N}/\text{ZnS}$ p - n junction as described in Sec. II B. Figure 9(a) shows the current-voltage characteristics of the p - n junction under dark conditions without illumination, indicating good diode rectification behavior with a current rectification ratio ($I_{1\text{V}}/I_{-1\text{V}}$) of 14. The large reverse-bias leakage current of 20 mA/cm^2 at -1 V is likely due to pinholes in the Cu_3N absorber layer giving rise to a low shunt resistance. Under illumination, however, the $\text{Cu}_3\text{N}/\text{ZnS}$ p - n junction does not generate any photocurrent, suggesting either limitations in carrier transport in the Cu_3N absorber layer due to defect states or energy barriers blocking carrier transport at the interfaces. From the inset of Fig. 9(a), linear current-voltage characteristics are observed for both Mo and In contacts on Cu_3N with current levels commensurate with the film resistivity and thickness, confirming that Mo serves as a good Ohmic contact for p -type Cu_3N .

To verify that there is no energy barrier inhibiting the transport of electrons (minority carriers) at the $\text{Cu}_3\text{N}/\text{ZnS}$ interface, photoelectron spectroscopy in air (PESA) was used to determine the ionization potential (VBM energy) of Cu_3N [Fig. 9(b)]. The threshold energy above which ultraviolet-wavelength photons are able to excite electrons from the VBM up to the vacuum level gives the ionization potential of Cu_3N . Extrapolating the onset of photoelectron yield to the energy axis in Fig. 9(b), the ionization potential of Cu_3N was deduced to be 5.1 eV, closely matching the experimental ionization potential value of 5.4 eV for Cu_3N in [3]. Adding the indirect band gap of 0.95 eV to the ionization potential of 5.1 eV gives an electron affinity (CBM energy) of 4.15 eV for Cu_3N , closely matched to the electron affinity of 3.9 eV for ZnS [43]. The small conduction band offset of 0.25 eV between Cu_3N and ZnS can allow electron transport across the $\text{Cu}_3\text{N}/\text{ZnS}$ interface. This is similar to the case of $\text{Zn}(\text{O},\text{S})$ buffer layers for $\text{Cu}(\text{In},\text{Ga})\text{Se}_2$ solar cells in which a conduction band offset of approximately 0.2 eV or smaller is needed

for collection of electrons through the p - n heterojunction interface [44]. Thus, having deduced that there are no barriers to carrier transport at both the $\text{Cu}_3\text{N}/\text{ZnS}$ and $\text{Cu}_3\text{N}/\text{Mo}$ interfaces, we conclude that the lack of photogenerated current in the $\text{Cu}_3\text{N}/\text{ZnS}$ p - n junction is due to defect states in the Cu_3N absorber layer inhibiting carrier transport. Based on our predictions from density functional theory and experimental evidence, we attribute the lack of photogenerated current to the large concentration of Cu_i defect states. Electrons (minority carriers in p -type Cu_3N) can be easily trapped by these Cu_i conduction band potential wells and subsequently recombine via Shockley-Read-Hall recombination, quenching the steady-state minority carrier concentration and the photogenerated current.

V. CONCLUSIONS

We have presented a comprehensive theoretical study of the electronic properties of point defects in Cu_3N using the state-of-the-art screened-exchange hybrid energy functional in conjunction with density functional theory. The calculations indicate that Cu_i interstitial defects have deep sub-band-gap (0/+) charge transition levels of 0.64 eV above the VBM and manifest as potential wells in the conduction band. Considering the low formation energy and large concentration of Cu_i defects, electrons can be efficiently captured at these defects leading to significant Shockley-Read-Hall recombination. Experimentally, we observe a distinct onset in optical absorption above photon energies of 0.65 eV, matching that of the Cu_i defects predicted by density functional theory. The experimentally measured lack of photoconductivity and photogenerated current in Cu_3N can be explained by the large concentration of Cu_i defects capturing electrons, causing substantial Shockley-Read-Hall recombination and quenching the steady-state minority carrier concentration under illumination.

ACKNOWLEDGMENTS

We are grateful for computing resources from the National Energy Research Scientific Computing Center (NERSC), DOE Office of Science User Facility supported by the Office of Science of the U.S. Department of Energy under Contract No. DE-AC02-05CH11231. In addition, we are thankful for computing resources from the NSF-funded NNIN Computing Facility at Stanford University. Visualization of the charge density difference plots was performed with VESTA [45]. The experimental section of this work was supported by the Department of Energy through the Bay Area Photovoltaic Consortium under Award No. DE-EE0004946. Part of this work was performed at the Stanford Nano Shared Facilities (SNSF), supported by the National Science Foundation under Award No. ECCS-1542152. Y.S.Y. thanks the Energy Innovation Programme Office Singapore (EIPO) and the National Research Foundation (NRF) Singapore for funding received through his Ph.D. scholarship. The Marcus and Amalia Wallenberg Foundation is acknowledged for funding A.H. through the Stig Hagström stipend.

APPENDIX

1. Image charge correction scheme for point defect formation energies

When performing calculations of point defects involving finite-size supercells with periodic boundary conditions, corrections to the total energies need to be applied to address the artificial electrostatic interactions between charged defects in periodic finite-size supercells. We have applied the Makov-Payne image charge correction scheme [46] to correct the HSE06 total energies for all calculations involving charged defects in Cu₃N. In this study, we have specifically applied an approximation to the Makov-Payne image charge correction scheme proposed by Lany and Zunger [26]:

$$\Delta E_{\text{MP}}(D, q) = (1 + f) \frac{q^2 \alpha_M}{2\epsilon L}, \quad (\text{A1})$$

where α_M is the lattice-dependent Madelung constant, ϵ is the static dielectric constant, and L is the linear supercell dimension $L = V_{\text{SC}}^{1/3}$. $(1 + f)$ is a scaling factor for the monopole correction, which is approximately 0.66. This image charge correction scheme has also been found to yield the most reasonable results in [2].

2. Methodology for estimating point defect concentrations

Using the methodology in [2,47,48], equilibrium defect concentrations in Cu₃N can be estimated using a Boltzmann distribution,

$$C[D, q] = N[D] \exp\left(\frac{-\Delta H_f[D, q]}{k_B T}\right), \quad (\text{A2})$$

where $C[D, q]$ is the concentration of defect D in charge state q , $N[D]$ is the number of possible defect sites, $\Delta H_f[D, q]$ is the formation energy of the defect, k_B is the Boltzmann constant, and T is the absolute temperature used in the growth of Cu₃N. Here we use $T = 433$ K, corresponding to the Cu₃N growth temperature in this study. The defect concentrations $C[D, q]$, free carrier concentrations, and equilibrium Fermi

level (E_F) are interdependent and have to be determined self-consistently using the charge neutrality condition,

$$p - n + \Sigma q C[D, q] = 0, \quad (\text{A3})$$

where p and n are the concentrations of free holes and electrons, respectively. The hole and electron concentrations p and n are calculated from the Fermi-Dirac distribution as

$$p = N_V \frac{1}{1 + [\exp(E_F - E_V)/k_B T]}, \quad (\text{A4})$$

$$n = N_C \frac{1}{1 + [\exp(E_C - E_F)/k_B T]}, \quad (\text{A5})$$

where N_C is the effective electron density of states in the conduction band and N_V is the effective hole density of states in the valence band. In the calculation of overall charge neutrality, we have used a degeneracy factor of 4 for acceptors and 2 for donors in the Fermi-Dirac distribution function. N_C and N_V are calculated as

$$N_C = 2 \left(\frac{2\pi m_{e,\text{DOS}}^* k_B T}{h^2} \right)^{3/2}, \quad (\text{A6})$$

$$N_V = 2 \left(\frac{2\pi m_{h,\text{DOS}}^* k_B T}{h^2} \right)^{3/2}, \quad (\text{A7})$$

where $m_{e,\text{DOS}}^*$ and $m_{h,\text{DOS}}^*$ are the electron and hole effective masses for DOS calculations. Since experimental values of $m_{e,\text{DOS}}^*$ and $m_{h,\text{DOS}}^*$ are unavailable, they are estimated as $m_{\text{DOS}}^* = g^{2/3} (m_l^* m_t^{*2})^{1/3}$ where g is a degeneracy factor for the number of constant-energy ellipsoids at the CBM or VBM within the first Brillouin zone (2 for the CBM and 1 for the VBM), and m_l^* and m_t^* are the longitudinal and transverse effective masses of the ellipsoids, respectively. By taking the second derivative of the energy eigenvalues $E_l(k)$ and $E_t(k)$ in the longitudinal and transverse directions within $\pm 0.01(2\pi/a)$ of the CBM at the M point (electrons) and VBM at the R point (holes), m_l^* and m_t^* are estimated as $\hbar^2/m_{l,t}^* = \pm d^2 E_{l,t}(k)/dk^2$ where $+$ ($-$) applies for the electrons (holes).

-
- [1] J. Kim, H. Hiroi, T. K. Todorov, O. Gunawan, M. Kuwahara, T. Gokmen, D. Nair, M. Hopstaken, B. Shin, Y. S. Lee, W. Wang, H. Sugimoto, and D. B. Mitzi, *Adv. Mater.* **26**, 7427 (2014).
- [2] Y. S. Yee, B. Magyari-Köpe, Y. Nishi, S. F. Bent, and B. M. Clemens, *Phys. Rev. B* **92**, 195201 (2015).
- [3] A. Zakutayev, C. M. Caskey, A. N. Fioretti, D. S. Ginley, J. Vidal, V. Stevanovic, E. Tea, and S. Lany, *J. Phys. Chem. Lett.* **5**, 1117 (2014).
- [4] J. E. Jaffe and A. Zunger, *Phys. Rev. B* **29**, 1882 (1984).
- [5] S.-H. Wei and A. Zunger, *Phys. Rev. B* **37**, 8958 (1988).
- [6] S. B. Zhang, S.-H. Wei, A. Zunger, and H. Katayama-Yoshida, *Phys. Rev. B* **57**, 9642 (1998).
- [7] A. Modin, K. O. Kvashnina, S. M. Butorin, L. Werme, J. Nordgren, S. Arapan, R. Ahuja, A. Fallberg, and M. Ottosson, *J. Phys.: Condens. Matter* **20**, 235212 (2008).
- [8] U. Hahn and W. Weber, *Phys. Rev. B* **53**, 12684 (1996).
- [9] J. Heyd, G. E. Scuseria, and M. Ernzerhof, *J. Chem. Phys.* **118**, 8207 (2003).
- [10] J. Heyd, G. E. Scuseria, and M. Ernzerhof, *J. Chem. Phys.* **124**, 219906 (2006).
- [11] T. M. Henderson, J. Paier, and G. E. Scuseria, *Advanced Calculations for Defects in Materials* (Wiley-VCH, Weinheim, 2011), p. 97.
- [12] A. Stroppa, G. Kresse, and A. Continenza, *Phys. Rev. B* **83**, 085201 (2011).
- [13] Z. Q. Liu, W. J. Wang, T. M. Wang, S. Chao, and S. K. Zheng, *Thin Solid Films* **325**, 55 (1998).
- [14] G. H. Yue, P. X. Yan, and J. Wang, *J. Cryst. Growth* **274**, 464 (2005).
- [15] T. Nosaka, M. Yoshitake, A. Okamoto, S. Ogawa, and Y. Nakayama, *Thin Solid Films* **348**, 8 (1999).
- [16] T. Maruyama and T. Morishita, *J. Appl. Phys.* **78**, 4104 (1995).
- [17] K. Matsuzaki, T. Okazaki, Y.-S. Lee, H. Hosono, and T. Susaki, *Appl. Phys. Lett.* **105**, 222102 (2014).
- [18] D. M. Borsa and D. O. Boerma, *Surf. Sci.* **548**, 95 (2004).

- [19] A. N. Fioretti, C. P. Schwartz, J. Vinson, D. Nordlund, D. Prendergast, A. C. Tamboli, C. M. Caskey, F. Tuomisto, F. Linez, S. T. Christensen, E. S. Toberer, S. Lany, and A. Zakutayev, *J. Appl. Phys.* **119**, 181508 (2016).
- [20] G. Kresse and J. Furthmüller, *Phys. Rev. B* **54**, 11169 (1996).
- [21] J. P. Perdew, K. Burke, and M. Ernzerhof, *Phys. Rev. Lett.* **77**, 3865 (1996).
- [22] P. E. Blöchl, *Phys. Rev. B* **50**, 17953 (1994).
- [23] M. Gajdoš, K. Hummer, G. Kresse, J. Furthmüller, and F. Bechstedt, *Phys. Rev. B* **73**, 045112 (2006).
- [24] A. F. Kohan, G. Ceder, D. Morgan, and C. G. Van de Walle, *Phys. Rev. B* **61**, 15019 (2000).
- [25] C. G. Van de Walle and Jörg Neugebauer, *J. Appl. Phys.* **95**, 3851 (2004).
- [26] S. Lany and A. Zunger, *Phys. Rev. B* **78**, 235104 (2008).
- [27] J. E. Jaffe and A. Zunger, *Phys. Rev. B* **64**, 241304(R) (2001).
- [28] J. R. Bakke, J. S. King, H. J. Jung, R. Sinclair, and S. F. Bent, *Thin Solid Films* **518**, 5400 (2010).
- [29] K. Vandewal, S. Albrecht, E. T. Hoke, K. R. Graham, J. Widmer, J. D. Douglas, M. Schubert, W. R. Mateker, J. T. Bloking, G. F. Burkhard, A. Sellinger, J. M. J. Fréchet, A. Amassian, M. K. Riede, M. D. McGehee, D. Neher and A. Salleo, *Nat. Mater.* **13**, 63 (2014).
- [30] P. E. Blöchl, O. Jepsen, and O. K. Andersen, *Phys. Rev. B* **49**, 16223 (1994).
- [31] C. M. Caskey, R. M. Richards, D. S. Ginley, and A. Zakutayev, *Mater. Horiz.* **1**, 424 (2014).
- [32] C. G. Van de Walle, *Wide-Band-Gap Semiconductors* (Elsevier Science Publishers B.V., Amsterdam, 1993), p. 406.
- [33] C. Ambrosch-Draxl and J. O. Sofo, *Comput. Phys. Commun.* **175**, 1 (2006).
- [34] C. Persson, *J. Appl. Phys.* **107**, 053710 (2010).
- [35] M. Birkett, C. N. Savory, A. N. Fioretti, P. Thompson, C. A. Muryn, A. D. Weerakkody, I. Z. Mitrovic, S. Hall, R. Treharne, V. R. Dhanak, D. O. Scanlon, A. Zakutayev, and T. D. Veal, *Phys. Rev. B* **95**, 115201 (2017).
- [36] J. Paier, M. Marsman, and Georg Kresse, *Phys. Rev. B* **78**, 121201(R) (2008).
- [37] M. Shishkin and G. Kresse, *Phys. Rev. B* **74**, 035101 (2006).
- [38] W. B. Jackson, N. M. Amer, A. C. Boccara, and D. Fournier, *Appl. Opt.* **20**, 1333 (1981).
- [39] U. Zammit, M. Marinelli, and R. Pizzoferrato, *J. Appl. Phys.* **69**, 3286 (1991).
- [40] R. Noriega, J. Rivnay, K. Vandewal, F. P. V. Koch, N. Stingelin, P. Smith, M. F. Toney, and A. Salleo, *Nat. Mater.* **12**, 1038 (2013).
- [41] D. R. Askeland, *The Science and Engineering of Materials* (Springer-Science+Business Media, Dordrecht, 1996), p. 717.
- [42] I. L. Repins, B. J. Stanbery, D. L. Young, S. S. Li, W. K. Metzger, C. L. Perkins, W. N. Shafarman, M. E. Beck, L. Chen, V. K. Kapur, D. Tarrant, M. D. Gonzalez, D. G. Jensen, T. J. Anderson, X. Wang, L. L. Kerr, B. Keyes, S. Asher, A. Delahoy, and B. Von Roedern, *Prog. Photovoltaics* **14**, 25 (2006).
- [43] R. K. Swank, *Phys. Rev.* **153**, 844 (1967).
- [44] C. Platzer-Björkman, T. Törndahl, D. Abou-Ras, J. Malmström, J. Kessler, and L. Stolt, *J. Appl. Phys.* **100**, 044506 (2006).
- [45] K. Momma and F. Izumi, *J. Appl. Crystallogr.* **41**, 653 (2008).
- [46] G. Makov and M. C. Payne, *Phys. Rev. B* **51**, 4014 (1995).
- [47] C. Persson, Y.-J. Zhao, S. Lany, and A. Zunger, *Phys. Rev. B* **72**, 035211 (2005).
- [48] Y. Kumagai, M. Choi, Y. Nose, and F. Oba, *Phys. Rev. B* **90**, 125202 (2014).